

Influence of Al-doping on the structural, magnetic, and electrical properties of $\text{La}_{1-x}\text{Ba}_x\text{Mn}_{1-x}\text{Al}_x\text{O}_3$ ($0 \leq x \leq 0.25$) manganites

J. Ardashti Saleh, I. Abdolhosseini Sarsari*, P. Kameli, and H. Salamati
*a) Department of Physics, Isfahan University of Technology,
 Isfahan, 84156-83111, Iran*

(Dated: August 4, 2021)

We have studied the effect of Al doping on the structural, magnetic and electrical properties of $\text{La}_{1-x}\text{Ba}_x\text{Mn}_{1-x}\text{Al}_x\text{O}_3$ ($0 \leq x \leq 0.25$) manganite, annealed in two 750°C and 1350°C temperatures. The XRD analysis shows that the structures in all samples have single phase rhombohedral structure with $R\bar{3}c$ space group. The unit cell volume almost decrease with increasing the Al doping in all samples. The grain growth with increasing annealing temperature and Al doping also have been studied. We observed that, T_c temperature decreases when the Al ion substitute in Mn ion site. The magnetic study of the samples via magnetic susceptibility results in Griffiths and spin-glass phase for samples doped with aluminium. Along the resistivity measurement results, the T_{MIT} (metal-insulator) transition temperatures decrease and the system become an insulator. The insulator-metal transition occurs for L0 sample in near 165K, while this transition is weak for H0 sample due to oxygen non-stoichiometry. Using three models viz. 1. Adiabatic small polaron hopping, 2. Variable range hopping, and 3. Percolation model, the resistance have been studied.

PACS numbers:

I. INTRODUCTION

During the last two decades, perovskite manganites are widely studied due to their interesting physical properties. Perovskite manganite with the formula $\text{A}_{1-x}\text{B}_x\text{MnO}_3$ (A is trivalent rare-earth cation such as La, Sm, Nd, Pr, ..., and B is divalent alkali or alkaline earth cation such as Sr, Ca, Ba or other vacancies) is any of a variety of manganese oxides with strongly correlated electrons¹⁻⁴. The doping in A and B sites provide cation size mismatch on ABO_3 perovskite manganites, measured by tolerance factor, that impact on the structures of the polycrystalline samples. Undoped LaMnO_3 , as a typical compound, is an antiferromagnetic (AFM) insulator. However, when part of La site is substituted by a divalent metal ion (like Ca, Ba or Sr), the compound becomes metallic ferromagnetic (FM) and introduce a ferromagnetic-paramagnetic (PM) transition (Curie temperature). Also a metal-semiconductor transition near the Curie temperature (T_C) could be found.

The fundamental feature of the magnetic properties and conductive mechanism in manganites can be explained qualitatively, by the double exchange (DE) mechanism, Jahn-Teller distortion and electron-phonon interactions in manganites. The DE mechanism is responsible for the ferromagnetic state due to transfer of itinerant e_g electron between the $\text{Mn}^{3+} - \text{O} - \text{Mn}^{4+}$ bond through the O^{2-} ion due to on-site Hund's coupling⁵⁻⁷. Jahn-Teller distortion which the structure will distort by removing the degeneracy of the e_g orbitals to stabilizes in the $3d_{3z^2-r^2}$ with respect to the $3d_{x^2-y^2}$ orbitals⁸. There is a direct link between the Jahn-Teller distortions and the polarons and this coupling is locally present in the metallic and insulating phases⁹.

To understand the structural, magnetic and transport properties of $\text{La}_{1-x}\text{A}_x\text{MnO}_3$ manganites, several studies have been reported on the doping of A-site with divalent ions¹⁰⁻¹⁴. A substitution at Mn (B-site) dramatically affects the structural, magnetic and transport properties of manganites. One of these compounds is $\text{La}_{1-x}\text{Ba}_x\text{MnO}_3$ (LBMO) manganite.¹⁵⁻¹⁹ As trivalent La^{3+} ions are replaced with a divalent Ba^{2+} in LaMnO_3 manganite, some of the manganese ion valence changed from Mn^{3+} (with the electronic configuration $3d^4, t_{2g}^3 e_g^1, S=2$) to Mn^{4+} (with the electronic configuration $3d^4, t_{2g}^3 e_g^0, S=3/2$) due to introducing holes into the this material. These holes permit charge transfer in the e_g state which is highly hybridized with the oxygen 2p state. In the following, the manganese ion valence can be change again by replacing the trivalent Al^{3+} ions instead of the trivalent Mn^{3+} ion²⁰. This case can cause a large changes in intended manganite. Al^{3+} does not possess a magnetic moment and do not participate in the magnetic interactions. Also the Al ion has a smaller size (0.535\AA) than that a Mn ion (0.645\AA) and makes increase in the structural stress^{15,20}. Based on the foregoing, the $\text{La}_{1-x}\text{Ba}_x\text{Mn}_{1-x}\text{Al}_x\text{O}_3$ manganite is one of the most attractive manganites. The $\text{La}_{1-x}\text{Ba}_x\text{Mn}_{1-x}\text{Al}_x\text{O}_3$ manganite having the T_C and T_N (Neel temperature) in the temperature range of $295 - 50$ K for doping range of $0 \leq x \leq 0.8$ ¹⁵.

Various models try to explain the conductive mechanism in perovskite manganites. Among these models we point out the variable range hopping (VRH), the adiabatic small polaron hopping (ASPH), percolation and Zhang models^{21,22}. The ASPH model offered for high temperature ($T > \frac{\theta_D}{2}$) resistivity in the paramagnetic regime at temperatures higher than T_C . θ_D is the Debye temperature and will be explained in the following. According to this model, the activation

energy E_0 is the depth of the local potential barrier of a trapped polaron²³.

The VRH model proposed to explain conduction mechanism for manganites via thermally activated small polarons in the adiabatic regime ($T < \frac{\theta_P}{2}$). In the VRH model the carriers are localized by random potential fluctuation. In percolation model, there is competition between FM and PM phases²¹, while according to Zhang model, a perovskite grain can be divided into a body phase and a surface phase in which the body phases have higher Curie temperature and magnetization²².

In this work, we investigate the effect of gradual B-site substitution by the Al^{3+} ion at the Mn-site in the $La_{0.80}Ba_{0.20}Mn_{1-x}Al_xO_3$ ($0 \leq x \leq 0.25$) compound. The changes in the structural, magnetic, and electrical properties of the $La_{0.80}^{3+}Ba_{0.20}^{2+}Mn_{0.8-x}^{3+}Mn_{0.2}^{4+}Al_x^{3+}O_3^2$ ($x = 0, 0.10, 0.15, 0.20, \text{ and } 0.25$) manganite polycrystalline samples have been reported by using XRD, ac magnetic susceptibility, and electrical resistivity measurements.

II. EXPERIMENT DETAILS

The $La_{1-x}Ba_xMn_{1-x}Al_xO_3$ samples ($x=0, 0.10, 0.15, 0.20, \text{ and } 0.25$) have been successfully prepared using sol-gel method. The required materials with purity of 99.9% are as follows:

$Ba_2(NO_3)_2$ (Barium nitrate), $La(NO_3)_3 \cdot 9H_2O$ (Lanthanum nitrate), $Mn(NO_3)_2 \cdot 4H_2O$ (Manganese nitrate), $Al(NO_3)_3 \cdot 9H_2O$ (Aluminum nitrate), $C_6H_8O_7$ (Citric acid), and $C_{10}H_{16}N_2O_8$ (Ethylene diamine tetra-acetic acid or EDTA).

The nitrates were dissolved in deionized water and mixed with EDTA and ultimately, pH adjusted to 7. The chemical equation for $x=0, 0.10, 0.15, 0.20, \text{ and } 0.25$ samples in $La_{1-x}Ba_xMn_{1-x}Al_xO_3$ is as following:

$$[\alpha La(NO_3)_3 \cdot 6 H_2O_{(aq)} + \beta Ba(NO_3)_2_{(aq)} + \gamma Mn(NO_3)_2 \cdot 4H_2O_{(aq)} + \sigma Al(NO_3)_3 \cdot 9H_2O_{(aq)}] + 3[\eta C_6H_8O_7 \cdot H_2O_{(aq)}] + 2[C_{10}H_{16}N_2O_8]_{(aq)} \rightarrow \phi La_{0.80}Ba_{0.20}Mn_{1-x}Al_xO_3_{(s)} + \omega CO_{2(g)} + \mu H_2O_{(g)} + \theta N_2_{(g)}$$

where, the Greek letters represent the amount of each compound. The molar ratio of acid, EDTA and nitrate materials were taken 1:2:3. The solution changed to a gel when it exposed to heat for drying the solution, (the temperature increased to $220^\circ C$ with rate of $\frac{1^\circ C}{6min}$). 2 hours Milling and 5 hours sintering at $450^\circ C$ result in homogenous composition.

Annealing at two different temperatures, $750^\circ C$ for 5 hours and $1350^\circ C$ for 48 hours, samples have a different grain size and grain boundaries (GBs) in these compounds. LBMO phases are beginning to grow at temperatures higher than $600^\circ C$ ²⁴. The slab samples were pressed under 354Psi (31.9MPa) pressure with typical dimensions of about $1.30 \times 3.22 \times 3.15 \text{ mm}^3$.

GBs growth, with increasing temperature from $750^\circ C$ to $1350^\circ C$, impact their magnetic and electrical properties. We demonstrate the slab samples with doping level of $x=0, 0.10, 0.15, 0.20, \text{ and } 0.25$ that annealed in $750^\circ C$ labeled: L0, L10, L15, L20, and L25 (L refers to low temperature), while those annealed in $1350^\circ C$ labeled: H0, H10, H15, H20, and H25 (H refers to high temperature), respectively.

Ultimately, we studied the structural, magnetic and electrical effects of Al doping on Mn sites in $La_{0.8}Ba_{0.2}Mn_{1-x}Al_xO_3$, by using XRD, SEM, ac susceptibility analysis and measuring the electrical resistance for two types of composition prepared at different temperatures. Phase formation and crystal structure of samples were studied by XRD pattern using $Cu-k\alpha$ radiation source with wavelength of $\lambda=1.5406 \text{ \AA}$ in the 2θ range from 20° to 80° , with a step size of 0.05° .

To study the magnetic properties of the samples, the ac susceptibility measurements were performed using a Lake Shore Ac Susceptometer (Model 7000) in 333Hz frequency and 800 A/m field. Also, we used conventional four probe method for measuring the electrical resistance by using a Laybold closed cycle refrigerator.

III. RESULTS AND DISCUSSION

Figure 1 shows the X-ray diffraction (XRD) patterns of $La_{0.8}Ba_{0.2}Mn_{1-x}Al_xO_3$ ($x=0-0.25$) at room temperature that were sintered at $1350^\circ C$ and $750^\circ C$. The XRD data was analyzed with Rietveld refinement using the FULLPROF software and Pseudo-Voigt function (for instance H0 sample's rietveld analysis was shown in Figure 2) and results show that the desired samples structure has approximately single phase with $R\bar{3}c$ space group belonging to the hexagonal structure where $a = b \neq c$. The results obtained from this analysis were collected in table I.

Figure 3 shows the changes in lattice parameters with increasing aluminum doping and annealing temperature. The a and b parameters decrease, c parameter, doesn't show regular behavior, c/a parameter increases and the unit cell volume decreases (except L15 and H25) with increasing Al doping. The c/a ratio represents a further increase in the length direction c than a and b are the unit cell parameters. It seems that reducing the unit cell volume is due to the fact that Al ions are smaller than Mn ions. (The radii of Al ion is 0.535 \AA and the Mn ion

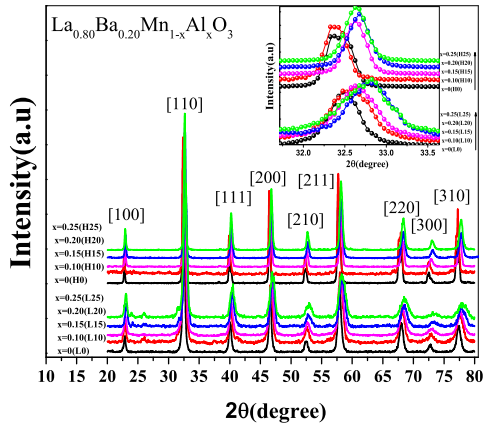


FIG. 1: The XRD pattern of all samples at room temperature that were sintered at in 750°C and 1350°C. Inset shows zoomed [110] peak. Can be seen a slightly shift to right hand side in all peak with increasing Al ion substitution.

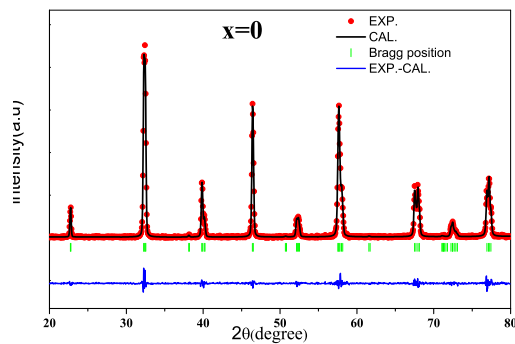


FIG. 2: The observed and calculated XRD patterns of H0 sample by Reitveld analysis. Red points (circle) shows the results of through experiments, black lines obtained from calculation, the blue line shows the difference between calculation and the results of experience and eventually green vertical lines, points out the Bragg positions.

is 0.645 Å)^{15,20}. By comparing the samples annealed at higher temperatures, it can be observed that all of lattice parameters increases with increasing annealing temperature. The reason for increasing in lattice parameters is the increasing concentration ratio of Mn^{3+}/Mn^{4+} . The Goldschmidt radius of Mn^{3+} (0.070nm) is much greater than that of Mn^{4+} (0.052 nm)²⁵. So this increase in the size of the lattice parameters can be attributed to the increase of Mn^{3+} ions due to increased oxygen deficiency with increasing annealing temperature²⁵.

The SEM images of slab samples for $x=0$ and $x=0.10$ (L0, H0, L10, and H10 samples) are shown in figure 4. Comparing the L0 to H0 and L10 to H10 in figure 4, the effect of annealing temperature on these samples can be well understood. The grains in samples L10 and H10 has grown more than samples L0 and L10, respectively. The average grain sizes of these samples are smaller than 5 μm .

The samples annealed in 1350°C (H0 and H10) are more homogeneous than samples that annealed in 750°C (L0 and L10). In general, decrease of grain surface energy by increasing the annealing temperature, is known as a driving force for migration of grain growth^{26,27}.

Grain size and their boundaries have impact on the magnetic and electrical properties of manganites¹⁴. It is observable that the average particle size of the samples increases by increasing the Al doping. It seems that doping of Al, cause the grain boundaries have more driving force for grain growth.

TABLE I: Lattice parameters and volumes, obtained from Rietveld refinement for all sample. R_{wp} , R_P and χ^2 are the fitting parameters in Rietveld refinement.

Sample-1350°C	a=b(Å)	c(Å)	c/a	V (Å ³)	R_{wp}	R_P	χ^2	Space group
x=0(L0)	5.5240	13.4690	2.4382	355.9375	18.7	14.9	1.43	R3c
x=0.10(L10)	5.4956	13.4418	2.4459	351.5755	24.0	20.3	1.48	R3c
x=0.15(L15)	5.4931	13.4995	2.4575	352.7649	17.6	13.0	1.30	R3c
x=0.20(L20)	5.4847	13.4838	2.4584	351.2793	24.2	17.7	1.44	R3c
x=0.25(L25)	5.4715	13.4840	2.4644	349.5863	24.9	18.7	1.75	R3c
x=0(H0)	5.5456	13.4700	2.4290	358.7500	18.8	11.6	1.01	R3c
x=0.10(H10)	5.5372	13.4720	2.4329	357.7200	29.7	23.2	1.21	R3c
x=0.15(H15)	5.5192	13.4350	2.4342	354.4400	16.9	10.1	1.10	R3c
x=0.20(H20)	5.5019	13.4130	2.4378	351.6400	17.9	12.7	1.11	R3c
x=0.25(H25)	5.4539	13.4590	2.4499	351.7500	18.2	11.7	1.18	R3c

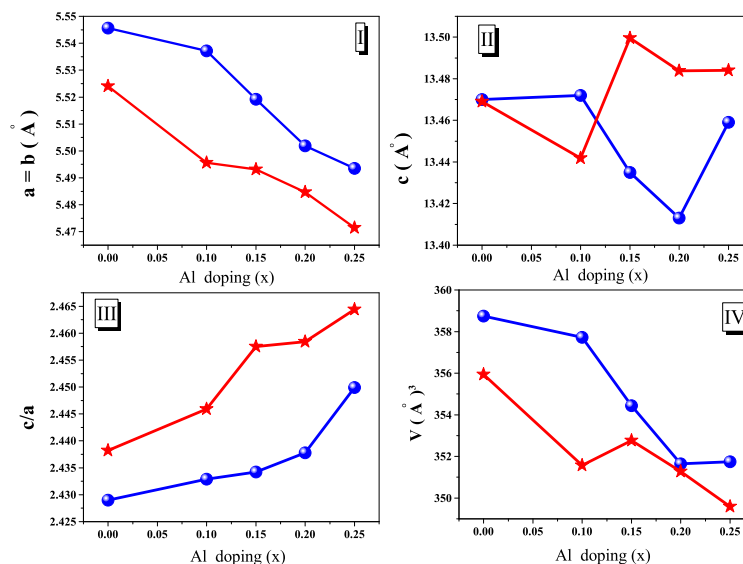


FIG. 3: Variation of (I) lattice parameters a and b, (II) lattice parameters c, (III) c/a ratio and (IV) unit cell volume, as a function of Al doping in $\text{La}_{0.8}\text{Ba}_{0.2}\text{Mn}_{1-x}\text{Al}_x\text{O}_3$ ($x=0-0.25$). The red star and blue circle points refer to samples that annealed in 750°C and 1350°C, respectively.

A. Magnetic properties

Measuring ac magnetic susceptibility, the magnetic properties of all samples studied. $\text{La}_{0.80}\text{Ba}_{0.20}\text{MnO}_3$ manganites show different magnetic transitions such as PM-FM or PM-AFM transitions and also FM to spin-glass state transition at different temperatures. ^{15,24,28,29} The heat treatment, level of synthesized temperature, annealing atmosphere and ..., could affect susceptibility of the samples, for a certain doping ^{24,30,31}.

Figure 5 shows the real parts of ac susceptibility for all samples. With decreasing temperature, magnetic entropy overcome to the thermal entropy and therefore below a certain temperature (Curie temperature, T_c) the samples show FM behavior. It can be seen that the Curie temperature decreases with increasing doping concentration. The decrease of the T_c with Al substitution has many reason such as 1- local cutoff magnetic interaction between the spins of t_{2g} electrons³². 2- Al^{3+} does not possess a magnetic moment and thus it should not participate in the magnetic interaction. This cause the ferromagnetic area reduction in ac susceptibility Vs temperature figure. 3- Al ion has smaller size than Mn ion and will cause an increase in structural stress with influence the magnetic and electronic properties of the mixed valence manganites.

The χ' shows downward slop below T_c for all samples (see Fig 5). Decreasing the temperature cause the immediate appearance of domain structure (The domain structure of ferromagnets is a result of minimizing the free energy)

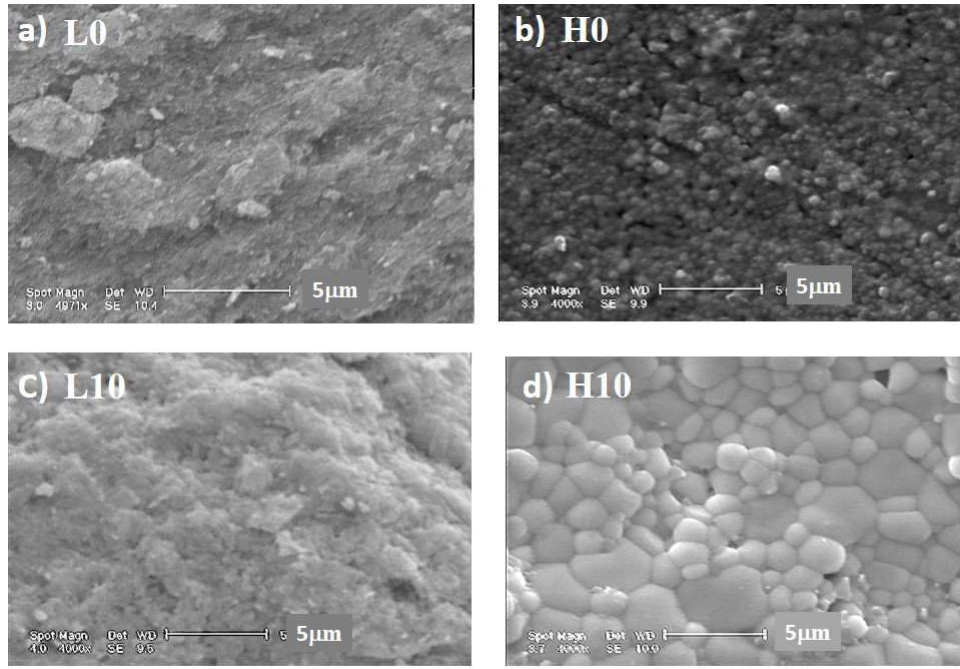


FIG. 4: SEM micrograph of $x=0$ and $x=0.10$ samples, a) L0, b) H0, c) L10 and d) H10 samples ($\text{La}_{0.8}\text{Ba}_{0.2}\text{Mn}_{1-x}\text{Al}_x\text{O}_3$) revealing the surface morphology and the particle size distribution at different sintering temperatures and Al doping.

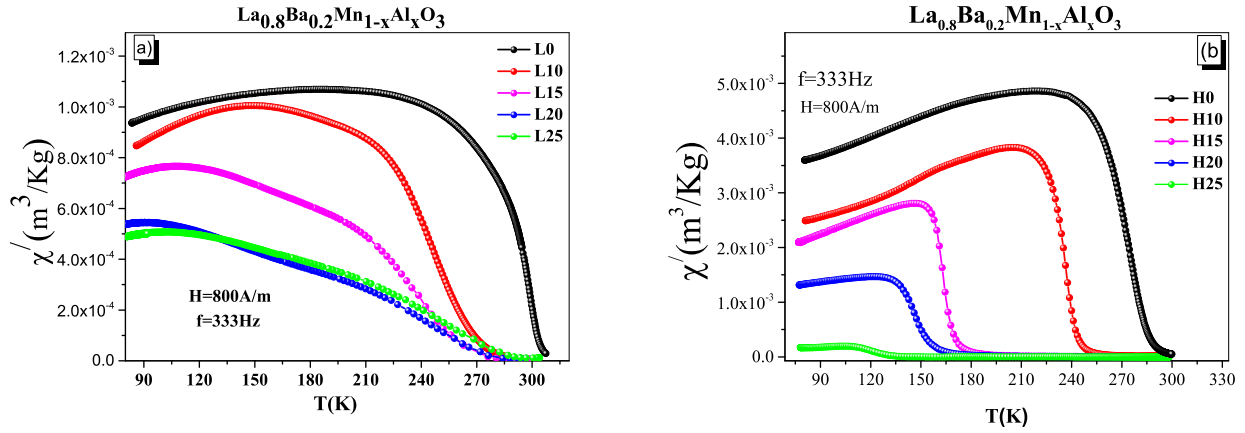


FIG. 5: Temperature dependence of (a) samples that annealed in 750°C and (b) samples that annealed in 1350°C for $x = 0-0.25$ samples in a magnetic field of 10 Oe and frequency of 333 Hz.

below T_c . However, by more reduction in temperature, samples lose their response to the ac magnetic field which could be responsible for the diminution of χ' (real part of the ac susceptibility) below T_c ³³. This χ' behavior can be justified by the change of domain wall movement (by applying small fields such as 10 Oe) and domain magnetization rotation (by applying large fields) in an ac applied magnetic field³³. Samples H10, H15, H20, H25 (samples annealed in 1350°C) and samples L15, L20 and L25 (samples annealed in 750°C) shows deviation from the Curie Weiss law (see Fig. 6). The Curie Weiss law is $\chi = \frac{C}{T - \theta_{cw}}$, where C is Curie constant and θ_{cw} is Curie-Weiss temperature. The θ_{cw} represents the molecular interaction between the moments.

This diversion proposed the short-range FM interactions or cluster spins formation¹⁵. In general, deviation of χ^{-1} , represents the Griffiths phase (GP) due to presence of FM clusters. Increasing temperature, these clusters participate in the paramagnetic phase, while above a certain temperature, that called Griffiths temperature, they totally disappear. The GP means the simultaneous presence of short-range FM clusters in the PM region, that is due

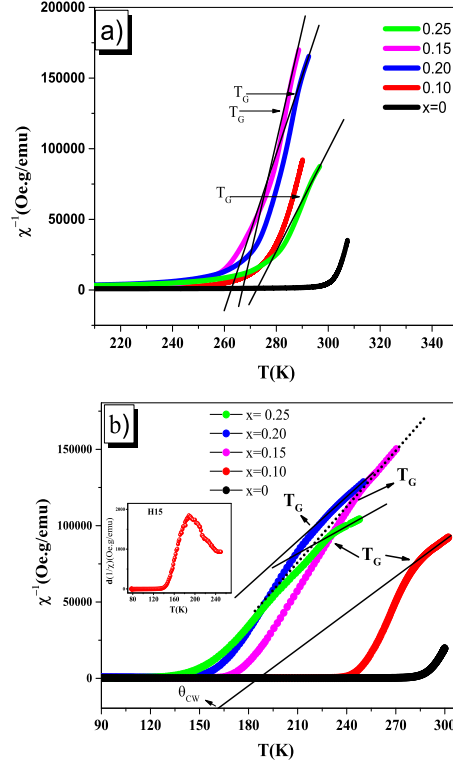


FIG. 6: Temperature dependence of the inverse magnetic susceptibility for a series of $\text{La}_{0.8}\text{Ba}_{0.2}\text{Mn}_{1-x}\text{Al}_x\text{O}_3$ ($0 \leq x \leq 0.25$) at $H=10$ Oe. a) and b) shows the inverse ac susceptibility obtained from magnetization measurements at $H=10$ Oe for samples that annealed in 750°C and 1350°C , respectively. All samples show the deviation from the Curie Weiss law (except L0, L10, and H0). Griffith temperature (T_G) is shown by arrows. θ_{CW} is the Curie Weiss temperature that shown for H10 as an example. Notice that the Griffiths temperature T_G is defined as the maximum of the $(d(1/\chi)/dT)(T)$ curves that shown as an example for H15 sample in the inset of part b.

to the dispersion of FM spin clusters in the PM domain³⁴. The Griffiths temperature (T_G) range is $T_c \leq T \leq T_G$ ³⁵. We used the Eq 1, to fit the intended experimental data. Also, the percentage of GP are obtained from Eq 2³⁶.

$$\chi^{-1} \propto (T - T_c^{rand})^{1-\lambda} \quad (1)$$

Where, T_c^{rand} is the critical temperature of the random ferromagnet where susceptibility diverges ($T_c^{rand} > T_c$), and λ is a positive quantity between 0 and 1³⁷. Zero refers to the PM regime.

$$GP\% = \frac{T_G - T_c}{T_c} \times 100\% \quad (2)$$

We have obtained the T_c^{rand} and λ parameters from equation 1 and the percentage of GP, from equation 2 listed in table II.

In many reports, the Griffiths phase was observed in Mn-site doping of LaMnO_3 perovskites³⁷⁻³⁹. Disorder caused by A⁴⁰ and B site doping⁴¹ and also controlling and elimination of oxygen vacancy²⁵, enhance the Griffiths state in a system. The decreasing in λ with Al^{3+} content indicates the further decrease in the GP properties and reveals that the size of the magnetic cluster decreases. It can be observed an increase in the quantity of λ for samples annealed at lower temperatures and irregular behavior for samples annealed at high temperature.

Figure 8 shows the $\frac{\theta_{CW}}{T_c}$ vs Al doping for all samples. The inset of this figure shows the T_c vs θ_{CW} . According to these results (Table II and figure 8), we can point out that; with Al^{3+} doping, amount of θ_{CW} reduced that would

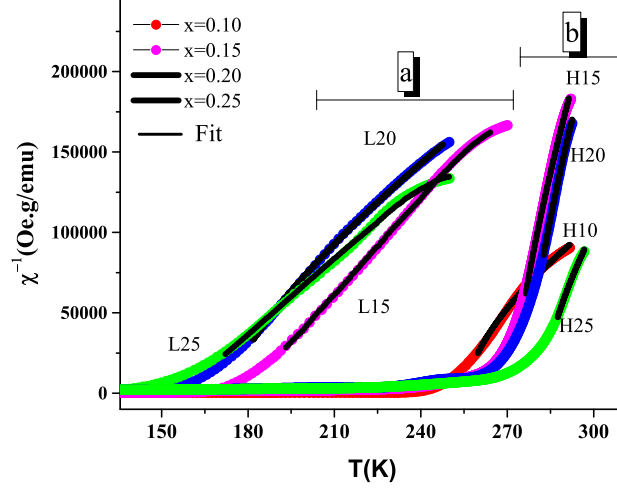


FIG. 7:

Inverse of magnetic susceptibility versus temperature for all samples of $\text{La}_{0.8}\text{Ba}_{0.2}\text{Mn}_{1-x}\text{Al}_x\text{O}_3$ ($0 \leq x \leq 0.25$) at $H=10$ Oe. a) and b) shows the samples that annealed in 1350°C and 750°C , respectively. The solid lines in the (a) and (b) part, show the fit with the power law equation $\chi^{-1} \propto (T - T_G)^{1-\lambda}$.

TABLE II: Parameters derived from fitting experimental curve for All sample(except L0,L10 and H0) from Eq 4 and Eq 7. T_c is Curie temperature, θ_p refers to Weiss temperature, T_c^{rand} refers to the disorder dependent FM ordering temperature, T_G refers to the Griffiths temperature, λ refers to the Griffiths exponent and $GP \times 100\%$ refers to the temperature range of Griffith phase. $Adj.R^2$ demonstrates the accuracy of matching equations 1 and 2 with the experimental data.

Sample-1350°C	T_c (K)	T_c^{rand}	θ_{CW} (K)	T_g (K)	λ	$GP \cdot \%$	$Adj \cdot R^2\%$
x=0(L0)	302	298
x=0.10(L10)	246	274
x=0.15 (L15)	242	272	264	288	0.286	19.0	99.78
x=0.20(L20)	245	277	258	285	0.305	16.3	99.85
x=0.25(L25)	272	282	266	290	0.377	6.6	99.84
x=0(H0)	274	277
x=0.10(H10)	236	256	161	275	0.389	16.5	99.50
x=0.15 (H15)	162	184	130	254	0.130	56.7	99.68
x=0.20(H20)	146	172	99	209	0.264	43.1	99.94
x=0.25 (H25)	119	161	14	233	0.139	95.7	99.57

means weakening of the DE interaction.³⁷ It is seen that the difference between T_c and θ_{CW} (the values of $\frac{\theta_{CW}}{T_c}$) increases with increasing Al doping for samples annealed at 1350°C due to the destruction of the FM order by the AFM interactions of the next-nearest neighbors⁴². In other words, the relationship between T_c and θ_{CW} when $\frac{\theta_{CW}}{T_c} < 1$ indicate the dominance of the AFM interactions in the $\text{La}_{0.8}\text{Ba}_{0.2}\text{Mn}_{1-x}\text{Al}_x\text{O}_3$ (H0, H10, H15, H20, and H25) samples. This case occurs in reverse order in samples that annealed at 750°C (L0, L10, L15, L20, and L25 samples).

Also we have observed spin glass (SG) behavior in sample H15 (sample with doping $x=0.15$ and annealed in 1350°C). Note that we believe that this effect could be seen in samples with higher doping, however just been brought for H15 sample as an example. One of the features of SG system is the dependence of its ac susceptibility on the applied field and frequency. In this sample, this behavior results in a sharp drop in the real part of the susceptibility at low temperatures, and the appearance of a peak in its imaginary part. The frequency-independent peaks termed as Hopkinson peaks are typical feature in many FM materials. But the second peak position shifts to higher temperatures with increasing frequency. So, to verify SG state presence, we have measured ac susceptibility of $\text{La}_{0.8}\text{Ba}_{0.2}\text{Mn}_{1-x}\text{Al}_x\text{O}_3$ ($x=0.15$) sample on the constant field and different frequencies.

Figure 9 shows the temperature dependence of the imaginary part (Out of phase) of ac susceptibility at different

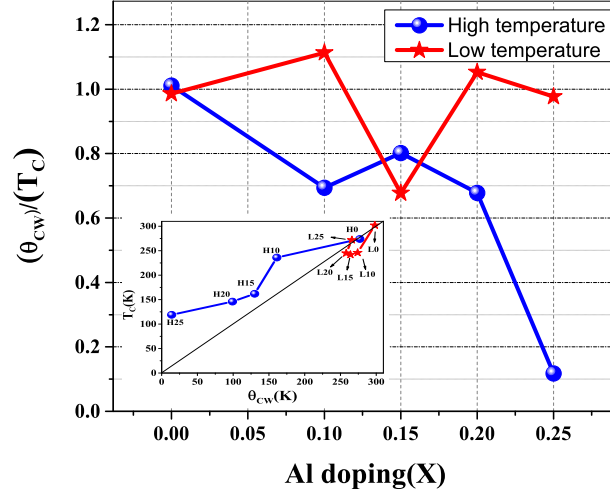


FIG. 8: This graph shows the $\frac{\theta_{CW}}{T_c}$ vs Al doping for all sample. The incet shows the T_c vs θ_{CW} .It can be seen that the difference between T_c and θ_{CW} is very less for samples that annealed in 750°C .

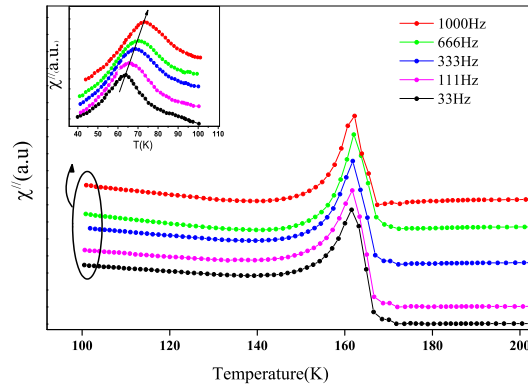


FIG. 9: The imaginary part of the susceptibility for H15 sample that measured at different frequencies. The inset shows the evolution of the peak by the increase of the frequency.

frequencies. The temperature dependences of susceptibility of this sample measured in an applied field of 10 Oe, after cooling in the zero field (ZFC). As can be seen from Figure 9, there is SG behavior below a certain temperature (see inset in Figure 9).

The first peak temperature that is frequency independent, represents the Curie temperature, while the second peak temperature, represents the freezing temperature T_f , that shifts towards higher temperatures with increasing frequency. This change by frequency is taken as the smoking gun for spin glasses. For further investigation of the SG nature at $x=0.15$ doping, we have checked the T_f 's dependence on frequency by conventional critical slowing down model which is as follows:

$$f = f_0 \left(\frac{T_f - T_g}{T_g} \right)^{z\nu} \quad (3)$$

Where, T_g is the dc value of T_f for $f \rightarrow 0$, f_0 is a constant in order of 10^9-10^{13} and $z\nu$ is dynamic critical exponent. The Fig 10 shows best fit of this model. The estimated values of $z\nu = 6.7$ and $T_g = 54\text{K}$ are within the realm of three dimensional SG system.

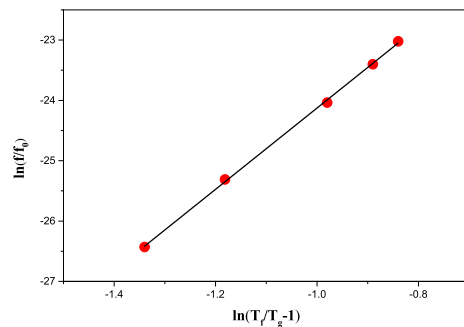


FIG. 10: Ln-Ln plot of the reduced temperature ($T_f / T_g - 1$) versus frequency for H15 sample.

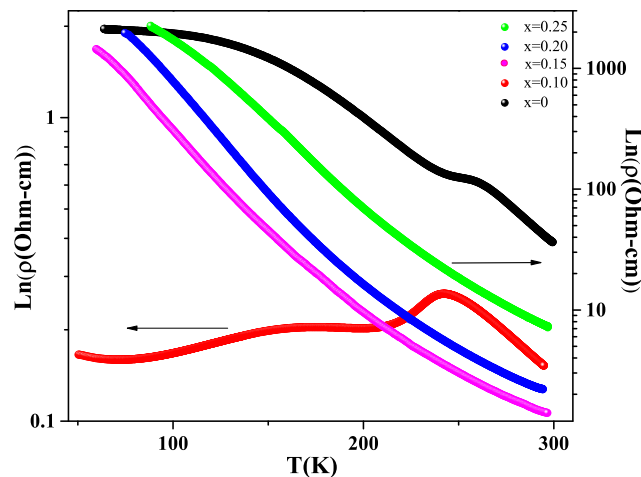


FIG. 11: Dependence of resistivity on temperature for $\text{La}_{0.8}\text{Ba}_{0.2}\text{Mn}_{1-x}\text{Al}_x\text{O}_3$ samples that annealed in high temperature. Resistivity increases with increasing aluminum doping among the high temperature samples. Only H0 and H10 samples show metal-insulator transition.

B. Electrical properties

Electrical transport measurement is one of the best methods for investigating the electrical properties of materials such as manganites. Thus to check the electrical resistance of samples, we used the closed circuit refrigerator and four probe method.

Figure 11 and 12 show the electrical resistivity of all samples. According to figure 11, for $x=0$ concentration, a poor metal-insulator transition can be seen at temperatures of about 259K that is corresponding to FM transition. This behavior is in agreement with $\text{La}_{0.81}\text{Ba}_{0.19}\text{MnO}_3$ in ref¹¹. This is probably due to that sample $x=0$, is approximately on the boundary of the insulator and metal state^{11,15}. The further doping shows insulator behavior ($x=0.19$), due to the oxygen vacancy or losing oxygen (According to figure 12, the ferromagnetic transition to the insulating state is completely occurred, and this transition becomes weak with increasing annealing temperature). This transition is in agreement with work Nagabhushana et al⁴³.

In reference⁴⁴, the effect of oxygen non-stoichiometry has been discussed and it has been shown that by increasing the amount of δ in $\text{O}_{3-\delta}$, the $\text{La}_{0.7}\text{Ba}_{0.3}\text{MnO}_{3-\delta}$ manganite shows insulation behavior. But figure 12, shows metal-insulators transition for $x=0$ in 170K. The reason for this issue can be attributed to the oxygen deficiency⁴³⁻⁴⁵. By increasing the amount of oxygen deficiency, the ratio of $\text{Mn}^{3+}/\text{Mn}^{4+}$ is reduced, which leads to decrease the transmission e_g interaction electrons. Studies have shown that the Curie temperature, T_c , depends on the mobility of e_g electrons, and the ratio of $\text{Mn}^{3+}/\text{Mn}^{4+}$, that is a key component to understanding the magnetoresistance effect and paramagnetic metal-ferromagnetic semiconductor transition^{44,46}. According to the Zener double exchange model, the

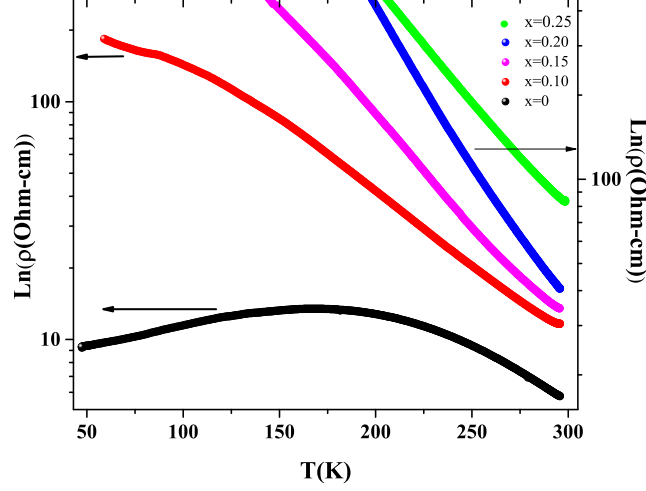


FIG. 12: Dependence of resistivity on temperature for $\text{La}_{0.8}\text{Ba}_{0.2}\text{Mn}_{1-x}\text{Al}_x\text{O}_3$ samples that annealed in low temperature. Resistivity increases with increasing aluminum doping among the low temperature samples. Only L0 sample show metal-insulator transition.

transfer of itinerant e_g electron between Mn^{3+} and Mn^{4+} ions through the O^{2-} ion, causing ferromagnetic interaction due to on-site Hund's coupling⁴⁷. When there are oxygen deficiency, the $\text{Mn}^{3+}/\text{Mn}^{4+}$ percent are changed. Also, By increasing the content of oxygen deficiency, the e_g electrons hopping probability and ferromagnetic region are reduced, that leads to decrease in the Curie temperature⁴⁸.

In other justification, annealing at higher temperature, the samples H0 lose more oxygen than L0 sample. This case is clear in Figure 12 in which there is a metal-insulator transition in 168K. With increasing annealing temperature, grain size increased and the surface to volume ratio decreased. At the same deoxygenated material, grain boundaries which effect by level of aluminium substitution on manganese site, play crucial role. According to Zhang model, the grain's surface is chaos and the curie temperature and metal-insulator transition temperature are less than the core phase²². Thus, the sample L0 has more surface area than H0, and as a result, the total Curie temperature is decreased because the Curie temperature of the surface phase are less.

The electrical resistance is insulating for samples $x=0.15$, 0.20 , and 0.25 (H15, H20, and H25). Increasing the non-magnetic Al^{3+} ion instead of the magnetic Mn^{3+} ions in lanthanum based perovskite manganites, reduces metal properties. The aluminium doping, as an impurity, decreases the polaron conductivity and increases the insulating properties of the system. Also increasing Al substitution (with smaller ionic radii size) instead of the Mn ion, led to increase stress. Such a structural changes in the lattice strain and deformations, affect the $\text{Mn}^{3+}\text{-OMn}^{4+}$ bond angle and length¹⁵. In addition, with increasing further doping, the tunnelling process at the grain boundaries (that acts as a potential barrier for charge carriers), are weakening. Also by doping the Al^{3+} , the content of Mn^{3+} are reduced progressively and thus power of DE reduced and this makes the ferromagnetic state weaker and system become insulator.

In a further analysis of electrical resistance, we used three ASPH, VRH, and percolation models. We used ASPH model to check the desired electrical properties of samples in zero applied magnetic field (see Figure 13: It is shown only for high annealed samples). In this model, which is also known as the Emin-Holstein theory of adiabatic small polaron hopping model⁴⁹, the conductivity data are dominated by the thermally activated hopping of small polarons in the high temperature ($T > T_{MIT}$) insulating phase⁵⁰:

$$\rho = \rho_\alpha T \exp\left(\frac{E_a}{K_B T}\right) \quad (4)$$

In Eq 4, parameter ρ_α is the coefficient independent of T. E_a and K_B are the activation energy and Boltzmann constant, respectively. Also, $\rho_\alpha = \frac{2K_B}{3ne^2a^2v_{ph}}$ is the residual resistivity, where e is the electronic charge, n is the density of charge carriers, a is the site-to-site hopping distance, and v_{ph} (in the order of 10^{13}Hz) is the longitudinal optical phonon frequency¹⁹. Also, we used $h\nu_{ph} = K_B\theta_D$ to calculate the optical phonon frequency. Here θ_D is the Debye temperature that was estimated from the experimental data in $\ln\rho/T$ versus $1/T$ plots by choosing the deviation point

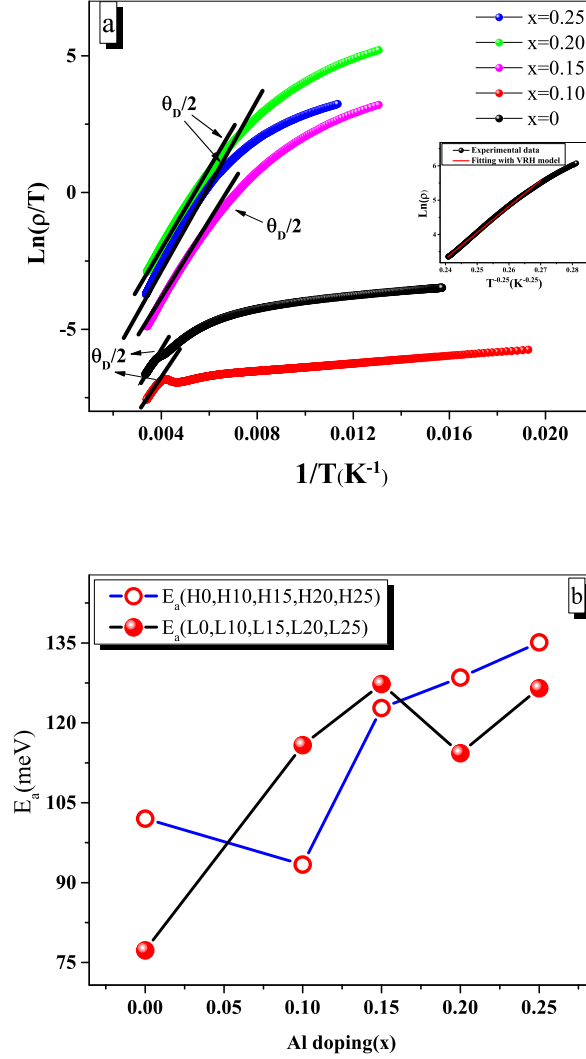


FIG. 13: (a) Theoretical fit of high temperature resistivity data for dependence of the $\ln(\rho/T)$ versus $1/T$. The solid lines represent the best fit of linear function. The inset of figure 13a shows the VRH model for H20 sample. (b) Activation energy E_a as a function of x for $\text{La}_{0.8}\text{Ba}_{0.2}\text{Mn}_{1-x}\text{Al}_x\text{O}_3$.

from linearity behavior. We calculated E_a for all samples in above T_{MIT} as a function of x using the equation 4, and plotted the results in Figure 13. Figure 13a clearly shows a linear dependence of $\ln(\rho/T)$ on $1/T$ above T_{MIT} for high temperature annealed samples. It can be seen from Figure 13b, that E_a has a minimum value of about 93.4 meV for H10 and 71meV for L0 samples. E_a increases with increasing x for high temperature annealed samples and increases with increasing x in the $0 < x < 0.15$ range and then decrease for L20 and L25 samples.

Also to understand the temperature dependence of electrical resistivity data in semiconducting region, we used VRH model. The expression for VRH model can be written as:

$$\rho = \rho_0 T \exp\left(\frac{T_0}{T}\right)^{1/4} \quad (5)$$

where ρ_0 is the Mott residual resistivity and T_0 is the Mott temperature which is expressed as $T_0 = 18\alpha^3/K_B N(E_F)$. Here $N(E_F)$ is the density of states (DOS) near the Fermi level, α is localization length and K_B is the Boltzmann constant. Inset of Fig 13a shows the fitting of the experimental data of $\ln\rho$ versus $T^{1/4}$ for H25 sample as an example. The values for $Adj \cdot R^2\%$ in Eqs. 4 and 5 are very close to 1. The table III includes the parameters of the VRH model.

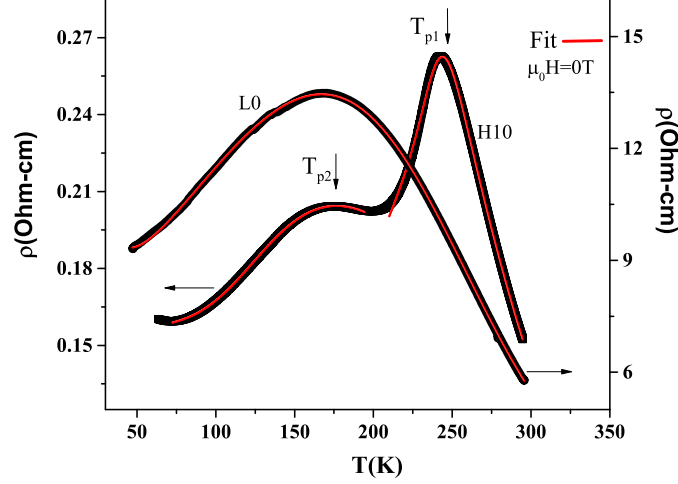


FIG. 14: Temperature dependence of the resistivity of $\text{La}_{0.8}\text{Ba}_{0.2}\text{Mn}_{1-x}\text{Al}_x\text{O}_3$ for L0 and H10 samples. The red solid line corresponds to the data fitted by Eq. 9.

TABLE III: Fitting parameters obtained from resistivity data for $\text{La}_{0.8}\text{Ba}_{0.2}\text{Mn}_{1-x}\text{Al}_x\text{O}_3$ samples by using VRH model. θ_D is the Debye temperature, ν_{ph} is the longitudinal optical phonon frequency, T_0 is the Mott temperature and $N(E_F)$ is the density of states (DOS) near the Fermi level.

Sample	(L0)	(L10)	(L15)	(L20)	(L25)	(H0)	(H10)	(H15)	(H20)	(H25)
E_a (meV)	77.3	115.8	127.3	114.3	126.5	102	93.4	122.8	128.5	135.1
θ_D (K)	535.5	467.3	437.6	475.3	476.3	526.3	514.1	293.8	335.6	363.6
$\nu_{ph} \times 10^{13}$	1.115	0.937	0.911	0.989	0.973	1.09	1.07	0.611	0.698	0.751
$T_0 \times 10^7$...	2.6	3.3	1.6	0.973	4.4	3.2	1.6
$N(E_F) \times 10^{24}$...	0.666	0.507	1.03	0.67	0.386	0.5311	1.06

TABLE IV: Matching parameters of electrical resistance graph of samples L0($x=0$) and H10($x=0.10$), by equation 9. The T_{p1} and T_{p2} are shown in Fig. 14.

Sample code	ρ_0 (Ωcm)	$\rho_2 \times 10^{-4}$ (ΩcmK^{-2})	$\rho_{4.5} \times 10^{-12}$ ($\Omega\text{cmK}^{-4.5}$)	ρ_α (ΩcmK^{-4})	E_a/K_B (meV)	T_c^{mod} (K)	Adj. $R^2\%$
$LBMA_0$ -L0	15.15	22.6	7.28	0.07	660.48	168	99.95
$LBMA_{0.10}$ -H10- T_{p1}	0.95	1.45	3.53	3.19	796.36	242	99.31
$LBMA_{0.10}$ -H10- T_{p2}	0.15	0.14	14.95	6.14×10^{-4}	301.52	172	99.69

Also to elucidate the transport properties in the whole temperature range, especially around the transition peak, we used percolation model for sample L0 and H10 (Because only these two dopings shows T_{MIT} in between all samples). In this model, the total resistivity is a sum of contributions from PM and FM regions, and at any temperature, ρ , is determined by the change of the volume fractions of both regions. In other words, in the percolation model, it is assumed that the ferromagnetic metallic and paramagnetic insulating regions are electrically linked in series and there exists a competition between these phases around the metal insulator transition temperature. The resistivity for the entire temperature range expressed as^{51,52}:

$$\rho = f\rho_{FM} + (1 - f)\rho_{PM} \quad (6)$$

Here ρ_{fm} is the temperature dependent electrical resistivity data that is given by:

$$\rho_{FM} = \rho_0 + \rho_2 T^2 + \rho_{4.5} T^{4.5} \quad (7)$$

Where the temperature independent part ρ_0 is the resistivity due to domain/grain boundary and refers to defects scattering. The $\rho_2 T^2$ term represents the electrical resistivity due to the electron-electron scattering process. The

term $\rho_{4.5}$ is a combination of electron- electron, electron-phonon and electron-magnon scattering processes^{53,54}. Also, ρ_{PM} is given by Eq. 4. As well as, f is the volume fraction of the FM phase and $(1 - f)$ is the volume fraction of the PM phase⁵⁵. Volume fractions of the FM and PM phases satisfy the Boltzmann distribution:

$$f = \frac{1}{1 + \exp(\frac{\Delta U}{K_B T})} \quad (8)$$

Where ΔU is the energy difference between FM and PM states and may be expressed as $\Delta U \approx -U_0(1 - \frac{T}{T_c^{mod}})$. In this expression, parameters U_0 is an energy difference of the quasi particles in the phase separated FM and PM states for a temperature well below T_c^{mod} temperature. T_c^{mod} means a temperature in the vicinity of which the resistivity has a maximum value. (It is near or equal to T_c) Thus the percolation model's formula given as:

$$\rho = \left(\frac{1}{1 + \exp(\frac{-U_0(1 - \frac{T}{T_c^{mod}})}{K_B T})} \right) (\rho_0 + \rho_2 T^2 + \rho_{4.5} T^{4.5}) + \left(\frac{\exp(\frac{-U_0(1 - \frac{T}{T_c^{mod}})}{K_B T})}{1 + \exp(\frac{-U_0(1 - \frac{T}{T_c^{mod}})}{K_B T})} \right) (\rho_\alpha T \exp(\frac{E_P}{K_B T})) \quad (9)$$

From equation 9, one can find that:

$\sqrt{f = 0}$ for $T \gg T_c^{mod}$, $f = 1$ for $T \ll T_c^{mod}$ and $f = f_c = 1/2$ at $T = T_c^{mod}$.

$\sqrt{1 - f = 1}$ for $T \gg T_c^{mod}$, $1 - f = 0$ for $T \ll T_c^{mod}$ and $1 - f = f_c = 1/2$ at $T = T_c^{mod}$.

where f_c is the percolation threshold. As a consequence, when $f < f_c$, the sample remains semiconducting and when $f > f_c$ it becomes metallic. Parameters ρ_0 , ρ_2 , $\rho_{4.5}$, ρ_α and E_P have been introduced previously. The red color solid line in Figure 14 shows the fitting results for the ρ - T curves obtained at zero field for the samples L0 and H10. All the available parameters obtained for samples that shows an insulator - metal transition (L0, H10), listed in Table IV, by using Eq 9 to fit the experimental data. These Values are consistent with values of previous works^{19,21,51}. It is worth mentioning that the percolation model is suitable to explain simultaneously the electrical transport of $\text{La}_{0.8}\text{Ba}_{0.2}\text{Mn}_{1-x}\text{Al}_x\text{O}_3$ (for samples that shows metal-insulator transition) in both ferromagnetic and paramagnetic areas.

IV. CONCLUSION

In summary, the effect of the Al substitution on the structural, magnetic, and electrical properties of $\text{La}_{1-x}\text{Ba}_x\text{Mn}_{1-x}\text{Al}_x\text{O}_3$ ($0 \leq x \leq 0.25$) manganites were investigated by XRD, Ac susceptibility and electrical resistivity measurements. We prepared two samples for each concentration, at temperatures of 750°C and 1350°C via sol-gel method. The XRD rietveld refinement indicates rhombohedral single phase structure with $R\bar{3}c$ space group. The lattice parameters and volume decrease with Al doping. The larger average grain size obtained due to aluminium doping and increasing annealing temperature. The ac magnetic susceptibility measurements show that the transition from paramagnetic (PM) to ferromagnetic (FM) phase at the Curie temperature, T_C , decreases from 274 K down to 119 K with increase in the Al doping level from $x = 0$ to $x = 0.25$ for samples annealed at 1350°C. In addition, the spin glass state exists in the $x = 0.15$ and higher level doping sample. This behavior indicates that the substitution of Al weakens the double exchange (DE) process. Also we observed a griffiths phase for some samples that annealed at 750°C and 1350°C. The temperature dependence of resistivity, $\rho(T)$, indicates that by increasing the Al doping level for samples annealed at 1350°C, the metal-insulator transition observed only for $x=0$ and $x=0.10$, while for $x=0$ there is a very weak metal-insulator transition, eventually the heavily doped samples become insulators. But for $x=0$ sample that annealed at 750°C, we observed the metal-insulator transition near 180K. We have attributed this effect to oxygen deficiency. To further analysis the dependence of resistivity on temperature we used three models (adiabatic small polaron hopping, variable range hopping and percolation model) for some samples. The $\rho(T)$ curve for the samples that shows metal-insulator transition was fitted with the percolation model, while the insulating region fitted with the adiabatic small polaron hopping at Paramagnetic state at $T > \frac{\theta_D}{2}$ (θ_D , Debye temperature) and the variable range hopping models at $T < \frac{\theta_D}{2}$.

V. ACKNOWLEDGEMENTS

This work was supported by Isfahan University of Technology (IUT).

-
- ¹ G. Jonker and J. Van Santen, *physica* **16**, 337 (1950).
 - ² T. Ramakrishnan, *Journal of Physics: Condensed Matter* **19**, 125211 (2007).
 - ³ Y. K. Lakshmi, S. Manjunathrao, and P. V. Reddy, *Materials Chemistry and Physics* **143**, 983 (2014).
 - ⁴ M.-H. Phan and S.-C. Yu, *Journal of Magnetism and Magnetic Materials* **308**, 325 (2007).
 - ⁵ C. Zener, *Physical Review* **82**, 403 (1951).
 - ⁶ P. W. Anderson and H. Hasegawa, *Physical Review* **100**, 675 (1955).
 - ⁷ E. Wollan and W. Koehler, *Physical Review* **100**, 545 (1955).
 - ⁸ D. Louca, T. Egami, E. Brosha, H. Röder, and A. Bishop, *Physical Review B* **56**, R8475 (1997).
 - ⁹ D. Louca, T. Egami, E. Brosha, H. Röder, and A. Bishop, *Physical Review B* **56**, R8475 (1997).
 - ¹⁰ L. M. Rodriguez-Martinez and J. P. Attfield, *Physical Review B* **54**, R15622 (1996).
 - ¹¹ H. Ju, Y. Nam, J. Lee, and H. Shin, *Journal of magnetism and magnetic materials* **219**, 1 (2000).
 - ¹² M. Kar and S. Ravi, *Materials Science and Engineering: B* **123**, 95 (2005).
 - ¹³ M. Lopez-Quintela, L. Hueso, J. Rivas, and F. Rivadulla, *Nanotechnology* **14**, 212 (2003).
 - ¹⁴ P. Kameli, H. Salamati, and A. Aezami, *Journal of Alloys and Compounds* **450**, 7 (2008).
 - ¹⁵ M. Narreto, H. Alagoz, J. Jeon, K. Chow, and J. Jung, *Journal of Applied Physics* **115**, 223905 (2014).
 - ¹⁶ B. Aslibeiki, P. Kameli, and H. Salamati, *Solid State Communications* **149**, 1274 (2009).
 - ¹⁷ J. S. Rathod, U. Khachar, R. Doshi, P. Solanki, and D. Kuberkar, *International Journal of Modern Physics B* **26**, 1250136 (2012).
 - ¹⁸ A. Abassi, N. Kallel, S. Kallel, and O. Peña, *Journal of Superconductivity and Novel Magnetism* **27**, 2353 (2014).
 - ¹⁹ A. Dhahri, M. Jemali, E. Dhahri, and E. Hlil, *Dalton Transactions* **44**, 5620 (2015).
 - ²⁰ R. Krishnan and A. Banerjee, *Journal of Physics: Condensed Matter* **12**, 3835 (2000).
 - ²¹ S. Manjunatha, A. Rao, T.-Y. Lin, C.-M. Chang, and Y.-K. Kuo, *Journal of Alloys and Compounds* **619**, 303 (2015).
 - ²² N. Zhang, W. Ding, W. Zhong, D. Xing, and Y. Du, *Physical Review B* **56**, 8138 (1997).
 - ²³ A. Chouket, O. Bidault, V. Optasanu, A. Cheikhrouhou, W. Cheikhrouhou-Koubaa, and M. Khitouni, *RSC Advances* **6**, 24543 (2016).
 - ²⁴ Z. Sadighi, A. Ataie, and M. Barati, *Powder Technology* **249**, 412 (2013).
 - ²⁵ H. Zhang, Y. Li, H. Liu, X. Dong, K. Chen, Q. Hou, and Q. Li, *Journal of superconductivity and novel magnetism* **25**, 2365 (2012).
 - ²⁶ E. Khzouz, A Major Qualifying Project Report Submitted to the Faculty of the WORCESTER POLYTECHNIC INSTITUTE Project Number: RDS **21381** (2011).
 - ²⁷ C. Yue, L. Zhang, S. Liao, and H. Gao, *Journal of materials engineering and performance* **19**, 112 (2010).
 - ²⁸ S. Trukhanov, L. Lobanovski, M. Bushinsky, I. Troyanchuk, and H. Szymczak, *Journal of Physics: Condensed Matter* **15**, 1783 (2003).
 - ²⁹ Y. G. Chukalkin, A. Teplykh, V. Voronin, A. Karkin, I. Berger, and B. Goshchitskii, *Physics of Metals and Metallography* **99**, 383 (2005).
 - ³⁰ W. Jiang, X. Zhou, G. Williams, Y. Mukovskii, and R. Privezentsev, *Journal of Applied Physics* **107** (2010).
 - ³¹ C. Chu, T. Li, H. Wang, and J. Wang, *Physica B: Condensed Matter* **405**, 4523 (2010).
 - ³² H. Qin, J. Hu, J. Chen, H. Niu, and L. Zhu, *Journal of magnetism and magnetic materials* **263**, 249 (2003).
 - ³³ E. Levin, V. Pecharsky, and K. Gschneidner, *Journal of Applied Physics* **90**, 6255 (2001).
 - ³⁴ A. Bray, *Physical review letters* **59**, 586 (1987).
 - ³⁵ P. Tong, B. Kim, D. Kwon, T. Qian, S.-I. Lee, S. Cheong, and B. G. Kim, *Physical Review B* **77**, 184432 (2008).
 - ³⁶ M. B. Salamon, P. Lin, and S. H. Chun, *Physical review letters* **88**, 197203 (2002).
 - ³⁷ P. Phong, L. Bau, L. Hoan, D. Manh, N. Phuc, and I.-J. Lee, *Journal of Alloys and Compounds* **645**, 243 (2015).
 - ³⁸ A. Abassi, N. Kallel, S. Kallel, and O. Peña, *Journal of Superconductivity and Novel Magnetism* **27**, 2353 (2014).
 - ³⁹ L. Joshi, V. Dayal, N. Rama, and S. Keshri, *Journal of Alloys and Compounds* **479**, 879 (2009).
 - ⁴⁰ N. Rama, M. R. Rao, V. Sankaranarayanan, P. Majewski, S. Gepraegs, M. Opel, and R. Gross, *Physical Review B* **70**, 224424 (2004).
 - ⁴¹ A. Pramanik and A. Banerjee, *Physical Review B* **81**, 024431 (2010).
 - ⁴² T. Arbuzova and Gizhevskii (????).
 - ⁴³ B. Nagabhushana, R. S. Chakradhar, K. Ramesh, C. Shivakumara, and G. Chandrappa, *Materials chemistry and physics* **102**, 47 (2007).
 - ⁴⁴ N. Abdelmoula, K. Guidara, A. Cheikh-Rouhou, E. Dhahri, and J. Joubert, *Journal of Solid State Chemistry* **151**, 139 (2000).
 - ⁴⁵ M. Lopez-Quintela, L. Hueso, J. Rivas, and F. Rivadulla, *Nanotechnology* **14**, 212 (2003).
 - ⁴⁶ S. Jin, T. H. Tiefel, M. McCormack, R. Fastnacht, R. Ramesh, and L. Chen, *Science* **264**, 413 (1994).
 - ⁴⁷ P. W. Anderson and H. Hasegawa, *Physical Review* **100**, 675 (1955).

- ⁴⁸ J. Yang, W. Song, R. Zhang, Y. Ma, B. Zhao, Z. Sheng, G. Zheng, J. Dai, and Y. Sun, *Solid state communications* **131**, 393 (2004).
- ⁴⁹ D. Emin and T. Holstein, *Physical Review Letters* **36**, 323 (1976).
- ⁵⁰ N. Mott and E. Davis, *Electronic process in nanocrystalline materials*, clarendon (1979).
- ⁵¹ G. Li, H.-D. Zhou, S. Feng, X.-J. Fan, X.-G. Li, and Z. Wang, *Journal of applied physics* **92**, 1406 (2002).
- ⁵² P. Phong, N. Khiem, N. Dai, D. Manh, L. Hong, and N. Phuc, *Journal of Magnetism and Magnetic Materials* **321**, 3330 (2009).
- ⁵³ P. Schiffer, A. Ramirez, W. Bao, and S. Cheong, *Physical Review Letters* **75**, 3336 (1995).
- ⁵⁴ G. J. Snyder, R. Hiskes, S. DiCarolis, M. Beasley, and T. Geballe, *Physical Review B* **53**, 14434 (1996).
- ⁵⁵ G. Li, H.-D. Zhou, S. Feng, X.-J. Fan, X.-G. Li, and Z. Wang, *Journal of applied physics* **92**, 1406 (2002).